A VSC-based Model for Power Flow Assessment of Multi-terminal VSC-HVDC Transmission Systems

Ricardo Martínez-Parrales, Claudio R. Fuerte-Esquivel, Boris A. Alcaide-Moreno, and Enrique Acha

***Abstract*—This paper puts forward a new practical voltage source converter (VSC) based AC-DC converter model suitable for conducting power flow assessment of multi-terminal VSC-based high-voltage direct current (VSC-MTDC) systems. The model uses an advanced method to handle the operational limits and control modes of VSCs into the power flow formulation. The new model is incorporated into a unified framework encompassing AC and DC power grids and is solved by using the Newton-Raphson method to enable quadratically convergent iterative solutions. The use of complementarity constraints, together with the Fischer-Burmeister function, is proposed to enable the seamless incorporation of operational control modes of VSC and automatic enforcement of any converter's operational limits that become violated during the iterative solution process. Thus, a dedicated process for checking limits is no longer required. Furthermore, all existing relationships between the VSC control laws and their operational limits are considered directly during the solution of the power flow problem. The applicability of the new model is demonstrated with numerical examples using various multi-terminal AC-DC transmission networks, one of which is a utility-sized power system.**

***Index Terms*—Complementarity constraint, current limit, high-voltage direct current (HVDC), voltage source converter (VSC), multi-terminal VSC-HVDC (VSC-MTDC) system, power flow.**

NOMENCLATURE

A. Sets and Indices

$\mathcal{N}_{AC}$	Set of AC nodes
$\mathcal{N}_{AC}^{PQ}$	Set of nonregulated AC nodes
$\mathcal{N}_{AC}^{PV}$	Set of *PV* nodes in AC grids
$\mathcal{N}_{AC}^{S}$	Set of slack nodes in AC grids
$\mathcal{N}_{DC}$	Set of all DC nodes
$\mathcal{N}_{DC}^{dc}$	Set of nodes at DC side of converter
$\mathcal{N}_{DC}^{P}$	Set of load nodes in DC grids
$j \in i$	Representation of all nodes j adjacent to node i
$(\cdot)^{\min}$, $(\cdot)^{\max}$	The minimum and maximum values
$(\cdot)^{sp}$	Specified value
$\overline{(\cdot)}$	Complex number
$(\cdot)_+$, $(\cdot)_-$	The upper and lower limits

B. Parameters

AC_{slack}	Slack converter control mode of AC grid
B_{ij}	Susceptance from nodes i to j
B_{pr}	Imaginary part of $\bar{Y}_{pr}$
B_{sf}	Imaginary part of $\bar{Y}_{sf}$
B_{sf}^{pr}	Imaginary part of $\bar{Y}_{sf}+\bar{Y}_{pr}$
G_{ij}	Conductance from nodes i to j
G_{pr}	Real part of $\bar{Y}_{pr}$
G_{sf}	Real part of $\bar{Y}_{sf}$
G_{sf}^{pr}	Real part of $\bar{Y}_{sf}+\bar{Y}_{pr}$
K	Modulation factor of voltage source converter (VSC)
P_i^{Gen}	Active power generated at AC node i
P_i^{Load}	Active power consumed at AC node i
P_{ij}^{sp}	Specified active power flow from nodes i to j
P_{nom}	Nominal power capacity of VSC
Q_i^{Gen}	Reactive power generated at AC node i
Q_i^{Load}	Reactive power consumed at AC node i
Q_{ij}^{sp}	Specified reactive power flow from nodes i to j
R	Conducting resistance of DC-DC converter
R_1	Conducting resistance of insulated gate bipolar transistor
V_i^{ref}	DC voltage droop control reference at node i
V_i^{sp}	Specified voltage magnitude at node i
VP^D	Voltage-power (*V-P*) droop control
VP_{db}^D	*V-P* droop control with dead band
$\boldsymbol{x}$	Vector of state variables
$\bar{Y}_{pr}$	Phase reactor admittance
$\bar{Y}_{sf}$	Shunt filter admittance
$\bar{Y}_T$	Transformer admittance

Manuscript received: February 7, 2021; accepted: June 29, 2021. Date of Crosscheck: June 29, 2021. Date of online publication: August 16, 2021.

This work was supported by the Fondo de Sustentabilidad Energética SENER-Conacyt, México (No. 246949 and No. 249795).

R. Martínez-Parrales and C. R. Fuerte-Esquivel (corresponding author) are with the Faculty of Electrical Engineering, Universidad Michoacana de San Nicolás de Hidalgo (UMSNH), Morelia, Michoacán, México (e-mail: rparrales@dep.fie.umich.mx, claudio.fuerte@umich.mx).

B. A. Alcaide-Moreno is with the National Center for Energy Control, Secretary of Energy, México (e-mail: boris.alcaide@cenace.gob.mx).

E. Acha is with the Department of Electrical Engineering, Tampere University (TU), Tampere FI-33720, Finland (e-mail: enrique.acha@tuni.fi).

DOI: 10.35833/MPCE.2021.000104

C. Variables

ϕ	Voltage phase angle of VSC
θ^{ref}	Reference voltage phase angle
θ_{ac}	Voltage phase angle at node *ac* of VSC
θ_i	Voltage phase angle at AC node *i*
D	Duty cycle of DC-DC converter
G_{sw}	Conductance of switching losses
I_{vsc}	VSC positive sequence current magnitude
$I_{vsc,d}^{des}$, $I_{vsc,q}^{des}$	*d*- and *q*-axis components VSC current before current limiter
$I_{vsc,d}^{ref}$, $I_{vsc,q}^{ref}$	*d*- and *q*-axis components VSC current after current limiter
m_a	Amplitude modulation index of VSC
$m_a^{(\cdot)}$	Modulation index used to control variable (·)
P_{ij}	Active power flow from nodes *i* to *j*
P_{loss}	Power loss of VSC
Q_{ij}	Reactive power flow from nodes *i* to *j*
Q_{vsc}	Reactive power generated by VSC
U_i	Voltage magnitude at DC node *i*
V_{ac}	Voltage magnitude at node *ac* of VSC
V_{dc}	Voltage magnitude at node *dc* of VSC
$\bar{V}_i$	Nodal complex voltage at AC node *i*
V_i	Voltage magnitude at AC node *i*
$x_{(\cdot)-}^{cc}$, $x_{(\cdot)+}^{cc}$	Complementary constraint auxiliary variables related to the lower and upper limits

I. Introduction

VOLTAGE source converters (VSCs) that comprise high-voltage direct current (HVDC) links represent the best solution to integrating large blocks of renewable energy into AC power grids, particularly offshore wind power [1]. In addition, direct current (DC) power transmission is moving in the direction of multi-terminal VSC-HVDC (VSC-MTDC) systems for unassailable reliability, where the VSC technology improves the operation flexibility through a fast and independent control of active and reactive power.

To quantify the manner in which VSC-based converter technology enables the flexible operation of MTDC systems, it is necessary to develop suitable mathematical VSC models, where the converter control characteristics and operational limits are duly incorporated. In this context, several proposals have aimed at modeling the steady-state characteristics of these systems. However, thus far, the control modes and operational limits of the converters have not been addressed in sufficient depth. This study fills this void and introduces a new VSC model, where the VSC operational limits and control modes are suitably combined in a unified framework and used to achieve quadratically convergent power flow solutions.

From the perspective of modeling, one approach has been to represent each converter station of the VSC-HVDC link by a controllable AC voltage source behind impedance, with the interaction of both converters represented through their common DC link by an active power flow constraint [2]-[4]. In these proposals, the magnitude and phase angle of the controllable voltage sources are combined with the nodal network state variables for a unified approach. The modulation of the complex voltage source within its operational limits enables the operational control mode specified for the converter station to be met. It should be noted that the proposals reported in [2] and [4] address neither VSC-MTDC structures nor DC circuit representation. On the other hand, [3] addresses the issue of MTDC systems but with no DC network representation. Three VSCs are considered, represented by controllable AC voltage sources that connect the AC bus via the inductive reactances of their corresponding coupling transformers. These converters share a common DC link when they are located in the same substation; otherwise, a DC network is formed. Two of these converters called primary converters operate under *PQ*- or *PV*-control mode. The third converter provides voltage control.

The generic model reported in [2] is used in [5] and [6] to solve the AC and DC power flow equations in a sequential fashion. In [5], these equations are associated with an AC electric network containing VSC-MTDC systems. All AC-DC converters embedded in the MTDC network can operate in either *PQ*- or *PV*-control mode except the one referred to as the DC slack converter. The former control mode is set to accomplish constant active and reactive power injections into the AC grid, whereas the aim of the latter one is to attain a constant active power injection and constant AC voltage magnitude at the system node. By contrast, the DC slack converter operates in a *QV* DC-control mode with its active power modulated to attain a constant DC voltage. In addition, the reactive power injected into the network is set to a fixed value. These control modes enable the decoupling and sequential solution of the AC and DC systems by representing the converter stations as constant power injection models. The inbound operation of each converter is assessed by checking its power limits at the system node, where these limits are expressed in terms of the converter current and voltage limits. Through the converter control modes reported in [5] and the controllable voltage source behind impedance proposed in [2], a unified power flow formulation is introduced in [7] to address the problem of multi-frequency AC systems interconnected by VSC-DC links. The VSC limits are expressed in terms of constraints of voltage and power at the AC terminal of converter and checked during the iterative solution process. Linear and nonlinear droop control characteristics are discussed in [8] for a distributed DC voltage control, where the converter limits are neglected.

An alternative VSC model, represented by a controllable AC voltage source and a controllable DC current source, is proposed in [9]. The analysis of MTDC networks considers different droop control strategies for the system frequency and DC voltage. In addition, the control action of the reactive power injected into the AC grid and the AC voltage magnitude of converter is performed through the controllable voltage source. Note that no converter limits are considered in the aforementioned study. In [10], a VSC-HVDC model comprising an active load and an ideal synchronous machine connected to a virtual node is proposed. The model parame-

ters are determined using a DC power flow study under the assumption that the active power at each converter terminal is known. This is followed by an AC power flow solution that uses the parameter values of each converter model and specified control modes: ① AC voltage magnitude, ② reactive power injection, and ③ amplitude modulation ratio. These controls rely on the concepts of voltage controlled- and load-type nodes.

In a VSC, the AC and DC voltages are related by the modulation index. Moreover, the DC-AC power conversion process may be represented by an ideal complex tap-changing transformer [11], where the tap magnitude represents the converter modulation index, which is used for controlling the AC voltage magnitude. On the other hand, the phase angle of the complex tap, which represents the voltage phase angle at the AC side of converter, is used for controlling the active power flowing through the VSC. The VSC capacity for injecting/absorbing reactive power into/from the AC grid is represented by a controllable shunt susceptance embedded at the AC terminal of converter. This VSC model has been used for representing back-to-back and point-to-point VSC-HVDC links in [12] and an MTDC ring in [13]. However, the control modes employed in [11]-[13] are quite basic, and the operational limits of the converters are neglected.

Based on the previous discussion and with the aim of filling the research void, this paper proposes a new VSC model in which a realistic representation of the steady-state operational characteristics and control operation modes is considered from the outset, bearing in mind the current limits of the converter stations. Within this context, the specific contributions of the VSC model presented in this study compared with existing models are given as follows.

When the VSC model is represented by a controllable AC voltage source, it is impossible to know the values of parameters that determine the VSC operational limits. This drawback is overcome in our model by including the VSC DC voltage, voltage phase angle at the AC side of converter, and the VSC modulation index as state variables.

The new VSC model includes the control modes of operation and operational limits within a unified formulation framework. In this case, the AC terminals of the VSC are explicitly modeled by separating its corresponding power flow mismatch equations from those associated with the common point of coupling. This enables the explicit representation of the VSC reactive power injected into/from the network together with its operational constraints. This reactive power internally generated by the VSC is modeled as a reactive power source Q_{vsc} and solved as a state variable to correctly constrain the solution to the current-based reactive power limits of the VSC. These limits are derived from the converter AC voltage magnitude and inner current controller of the VSC. Note that the representation of the VSC reactive power by variable shunt susceptance [11] leads to inaccurate results for an operation outside its limits.

Unlike the approaches presented in [2]-[13], the VSC control system is represented by an inner current control loop and several outer mode controls, all of which are used in practical applications. The inner and outer controls are related through a set of complementarity-based control constraints to consider the interaction between control modes during the power flow solution process.

The VSC limit revision presented in [2]-[13] is conducted using the direct control method, and only [5] and [7] check the VSC current limits to avoid the overloading of switches. Unlike the methods in [2]-[13], in this study, the VSC current limits are based on a vector control, also known as *dq* decoupled control. These current limits are checked by using two current limiter techniques and are converted into equivalent constraints of active and reactive power limits, which are automatically monitored during the iterative solution process to avoid an overcurrent condition in the converter station.

Unlike [2]-[13], the converter DC voltage limits representing the DC capacitor charging limits and the modulation index limits representing the converter design limitations are considered in this model. This prevents the power flow results from lacking a physical meaning.

The complementarity constraint concept together with the Fischer-Burmeister merit function (FBMF) has been envisioned as an attractive approach for directly including the operational limits of equipment into the power flow problem [14]-[17]. This study proposes the application of these concepts to the VSC operational limits. This manner of modeling the VSC steady-state operation permits us to state directly the existing relationships between the control laws and operational limits of the VSC in a single framework of analysis. In this case, the double-sided inequality constraints representing the VSC limits are transformed into equality constraints by using the complementarity condition approach and FBMF. The ensuing set of constraints together with the complementarity-based control constraints are directly added to the set of power flow mismatch equations for performing the automatic checking of the VSC operational limits and, when applicable, the automatic enforcement during the iterative solution process. Thus, the if-based conditional tests for checking violated limits used in [2]-[13] are avoided. Note that with the proposed method, the solution process through a numerical solver will automatically limit any variable outside bounds. However, a limit checking using if-based conditional tests is possible only after obtaining the power flow solution, as no access to the numerical solver's code is available. In this case, the power flow study must be repeated until no limit violations exist.

The stated individual contributions form the basis of an extended formulation to encompass multi-terminal VSC-based AC-DC power flow solutions in which all the VSC control variables such as the modulation index, converter phase angle, and VSC control modes of operation are combined with the state variables associated with the AC and DC grids for unified iterative solutions.

The remainder of the paper is organized as follows. The steady-state VSC model is elaborated in Section II. Section III details the representation of the VSC operational limits by means of equality constraints. The formulation and solution method of the multi-terminal AC-DC power flow problem is detailed in Section IV. Illustrative examples are pre-

sented in Section V, which emphasizes the performance of the new VSC-MTDC model. Section VI provides concluding remarks.

II. VSC-BASED AC-DC STATION MODEL

The derivation of the mathematical model representing the VSC steady-state operation is also based on the concept of an ideal complex tap-changing transformer [11], with the converter's schematic representation shown in Fig. 1. The differences with respect to the model proposed in [11] seem minor, but they are in fact very subtle and critical to the main emphasis of this study, namely, the incorporation of design and operational limits in the VSC power flow model. Noteworthy is the use of a synchronous voltage source, which replaces the variable shunt susceptance used in [11]. As explained in Section I, the representation of the VSC reactive power by variable shunt susceptance leads to inaccurate results for an operation outside the limits.

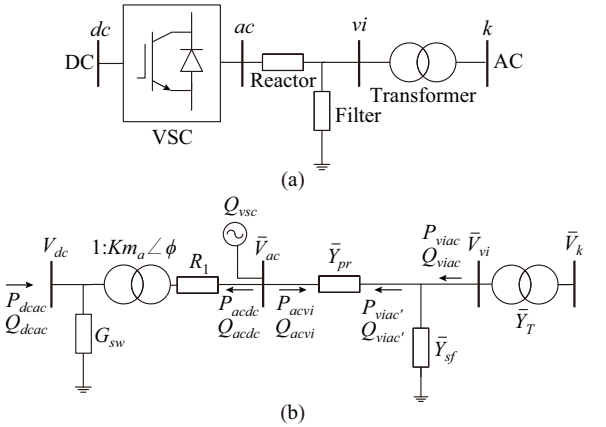

Fig. 1. AC-DC converter station and transformer. (a) Schematic representation. (b) Positive-sequence equivalent circuit model.

A. VSC Power Equations

Based on the equivalent circuit of VSC shown in Fig. 1, the power flow equations associated with its steady-state operation are expressed as:

$$P_{dcac}(\boldsymbol{x})=V_{dc}^2\left(G_{sw}+K^2m_a^2\frac{1}{R_1}\right)-Km_aV_{dc}V_{ac}\frac{1}{R_1}\cos\left(\phi-\theta_{ac}\right) \quad (1)$$

$$Q_{dcac}(\boldsymbol{x})=-Km_aV_{dc}V_{ac}\frac{1}{R_1}\sin\left(\phi-\theta_{ac}\right) \quad (2)$$

$$P_{acdc}(\boldsymbol{x})=\frac{1}{R_1}V_{ac}^2-Km_aV_{dc}V_{ac}\frac{1}{R_1}\cos\left(\theta_{ac}-\phi\right) \quad (3)$$

$$Q_{acdc}(\boldsymbol{x})=-Km_aV_{dc}V_{ac}\frac{1}{R_1}\sin\left(\theta_{ac}-\phi\right) \quad (4)$$

$$P_{viac}(\boldsymbol{x})=G_{sf}^{pr}V_{vi}^2+V_{vi}V_{ac}\left(G_{pr}\cos\left(\theta_{vi}-\theta_{ac}\right)+B_{pr}\sin\left(\theta_{vi}-\theta_{ac}\right)\right) \quad (5)$$

$$Q_{viac}(\boldsymbol{x})=-B_{sf}^{pr}V_{vi}^2+V_{vi}V_{ac}\left(G_{pr}\sin\left(\theta_{vi}-\theta_{ac}\right)-B_{pr}\cos\left(\theta_{vi}-\theta_{ac}\right)\right) \quad (6)$$

$$P_{acvi}(\boldsymbol{x})=-G_{pr}V_{ac}^2+V_{ac}V_{vi}\left(G_{pr}\cos\left(\theta_{ac}-\theta_{vi}\right)+B_{pr}\sin\left(\theta_{ac}-\theta_{vi}\right)\right) \quad (7)$$

$$Q_{acvi}(\boldsymbol{x})=B_{pr}V_{ac}^2+V_{ac}V_{vi}\left(G_{pr}\sin\left(\theta_{ac}-\theta_{vi}\right)-B_{pr}\cos\left(\theta_{ac}-\theta_{vi}\right)\right) \quad (8)$$

The value of $K=\sqrt{3/2}$ is used to represent the relationship between the DC voltage and line-to-line root-mean-square (RMS) voltage at the VSC ends.

In the context of converter power losses, the series resistance R_1 represents the ohmic losses, and the conductance G_{sw} represents switching losses. Note that when a more accurate equation for obtaining the VSC power losses is available, i.e., f_{loss}, this equation can be directly integrated into the proposed formulation by iteratively modifying the value of G_{sw} as $G_{sw}^k=G_{sw}^{k-1}+\left[f_{loss}-\left(P_{dcac}(x)+P_{acdc}(x)\right)\right]/V_{dc}^2$.

The VSC operation involves the direct control of two state variables, i.e., the amplitude modulation index m_a and VSC phase angle ϕ, which allows the control of the magnitude and phase angle of the VSC voltage at the AC side $\bar{V}_{ac}$, respectively. Finally, since $\theta_{ac}=\phi$ at the power flow solution, $Q_{dcac}=Q_{acdc}=0$ is followed from (2) and (4).

B. Control Modes of Operation

The control system of a VSC-based converter is based on an inner current control loop that controls the AC current and a set of outer controllers that supply the AC current reference values in the *dq*-frame for the inner current controller.

The choice of outer controllers depends on the desired control modes of operation for the VSC. In this context, the control targets are met by regulating the VSC voltage output $\bar{V}_{ac}$ with respect to the nodal voltage $\bar{V}_{vi}$ through the independent control of m_a and ϕ. Thus, several control modes can be set as follows.

1) Control Through Modulation Index m_a

The magnitude of $\bar{V}_{ac}$ is adjusted through the modulation index m_a to achieve one of the following control actions: ① to maintain the voltage magnitude of $\bar{V}_{vi}$ at a given set point V_{vi}^{sp} by injecting or extracting the necessary reactive power; ② to ensure that the reactive power is exchanged with the AC grid to a specified value Q_{viac}^{sp}. These two control modes are performed as long as the modulation index is within its limit values. If a limit violation occurs, then the modulation index is fixed at that limit, and the controlled variable is freed. In this situation, the possible values of freed variable depend on the reactive power limits of VSC.

2) Control Through Phase Angle ϕ

Three VSC control strategies can be specified by regulating the phase angle of $\bar{V}_{ac}$ through the phase angle ϕ. The first control action consists of maintaining a specified active power flow through the converter, where this power flow can be set to a constant value (i.e., $P_{dcac}(\boldsymbol{x})=P_{dcac}^{sp}$), or to a value that depends on the type of DC voltage droop control used for the VSC (i.e., $P_{dcac}(\boldsymbol{x})=P_{dcac}^{sp}(V_{dc}^{ref})$). In this latter case, three control approaches are considered: ① voltage-power (*V-P*) droop; ② voltage-current (*V-I*) droop; ③ *V-P* droop with a dead band. The corresponding equations for $P_{dcac}^{sp}(V_{dc}^{ref})$ are given in Section III of [8]. For cases where no limit violations occur in the DC voltage value V_{dc}, the active power is controlled. However, when the DC voltage is set to one of its limits, the range of the active power without vio-

lating the VSC capability depends on its current control.

The second control mode is associated with the voltage regulation at the DC side of converter to a specified value of V_{dc}^{sp} by injecting or extracting the required active power $P_{dcac}(\boldsymbol{x})$. In this case, the converter becomes a DC grid slack converter because it will maintain the power balance and the capacitor charge of the DC grid.

In the last control strategy, the converter transfers the necessary active power $P_{dcac}(\boldsymbol{x})$ to achieve an active power balance in the AC grid. In this case, the VSC can be regarded as an AC grid slack converter. In order to avoid convergence problems, these two slack control modes are not limited in the proposed formulation.

3) Control Modes of VSC

Based on the several control modes mentioned above, the VSC can operate in six different control modes, i. e, V_{vi}^{sp}–$P_{dcac}^{sp}(\boldsymbol{x})$, Q_{viac}^{sp}–$P_{dcac}^{sp}(\boldsymbol{x})$, V_{vi}^{sp}–V_{dc}^{sp}, Q_{viac}^{sp}–V_{dc}^{sp}, V_{vi}^{sp}–AC_{slack}, and Q_{viac}^{sp}–AC_{slack}.

C. VSC Limits

To guarantee that the power flow solution corresponds to a feasible steady-state operation of VSC, three limiting factors must be considered in the formulation: ① the upper and lower charge limits of DC capacitor; ② the operating range of modulation index; ③ the maximum continuous current $I_{vsc}^{\max}$ that the switching elements of converter can handle [18]. The first two operational limits are considered by the inequality constraints $V_{dc}^{\min} \le V_{dc} \le V_{dc}^{\max}$ and $m_a^{\min} \le m_a \le m_a^{\max}$. Conversely, the VSC protection against overcurrents is expressed in terms of the maximum apparent power $S_{acvi}^{\max} = I_{vsc}^{\max} V_{ac}$ at which the converter can operate. This power is decomposed to obtain the lower and upper limits $Q_{vsc}^{\min} \le Q_{vsc} \le Q_{vsc}^{\max}$ and $P_{dcac}^{\min} \le P_{dcac}(\boldsymbol{x}) \le P_{dcac}^{\max}$ based on the manner in which the AC current of converter is maintained within limits, i.e., the inner current limiter technique. The mathematical expressions for the active and reactive power limits are derived from the current control scheme.

The current control scheme applied to the VSC is shown in Fig. 2.

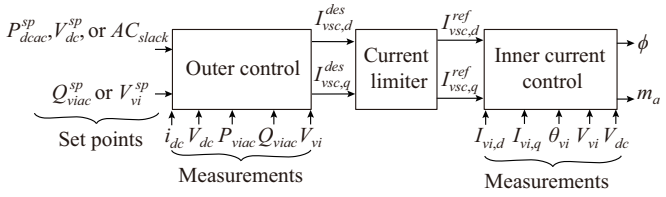

Fig. 2. Current control scheme.

The outer control of converter defines the desired *d*- and *q*-axis components of the AC current, denoted as $I_{vsc,d}^{des}$ and $I_{vsc,q}^{des}$, respectively, based on the values of active and reactive power required to achieve the control targets. A current limiter control module receives and adjusts both *d*- and *q*-axis components of the desired current to ensure that the converter will not operate in an overcurrent condition. Finally, the current limiter supplies the reference values of both *d*- and *q*-axis currents to the inner current control to adjust the modulation index m_a and phase angle ϕ. How these controllers operate dynamically is out of the scope of this study but can be found in [18], [19].

1) Current Limiter Control

By considering a voltage invariant transformation between the frames of reference *abc* and *dq*0, a phase-locked loop connected to phase A of node *vi*, and a balanced three-phase system, the constant voltages and currents in the *dq* framework can be directly related to the positive-sequence active and reactive power. In this case, the active and reactive power $P_{viac'}$ and $Q_{viac'}$ as shown in Fig. 1, are mathematically expressed in terms of voltages and currents in the *dq* framework by $P_{viac'} = 1.5 V_{vi,d} I_{vsc,d}$ and $Q_{viac'} = -1.5 V_{vi,d} I_{vsc,q}$, respectively. In this case, $V_{vi,d} = \sqrt{2/3}\, V_{vi}$ is the direct component of voltage magnitude at node *vi*. In addition, $I_{vsc,d}$ and $I_{vsc,q}$ are the *d*- and *q*-axis currents of converter in the *dq* framework, respectively, where $\left| I_{vsc,d} + \mathrm{j} I_{vsc,q} \right| = I_{vsc,dq} = \sqrt{2/3}\, I_{vsc}$, and I_{vsc} is the total current flowing through the VSC such that $I_{vsc,dq}^{\max} = \sqrt{2/3}\, I_{vsc}^{\max}$.

Based on this transformation of coordinates, the *d*- and *q*-axis components of the desired current at the k^{th} iteration of the power flow solution process are calculated as:

$$I_{vsc,d}^{des,k} = \frac{P_{viac'}^{k}}{1.5 V_{vi,d}^{k}} \tag{9}$$

$$I_{vsc,q}^{des,k} = \frac{-Q_{viac'}^{k}}{1.5 V_{vi,d}^{k}} \tag{10}$$

For the sake of simplicity, the upper index *k* is removed under the assumption that the magnitudes of all currents are calculated at each Newton-Raphson iteration.

The desired current of the VSC $I_{vsc,dq}^{des} = \sqrt{\left(I_{vsc,d}^{des}\right)^2 + \left(I_{vsc,q}^{des}\right)^2}$ is always constrained to $I_{vsc,dq}^{des} \le I_{vsc,dq}^{\max}$ by the current limiter control module. The current limiter technique can be in a vector form to satisfy this constraint, as detailed in [20]. In this case, the *d*- and *q*-axis components of the desired current are scaled down in the same proportion to maintain the converter current within its limit, as shown in Fig. 3(a). Thus, the *d*- and *q*-axis components of $I_{vsc,dq}^{des}$ are scaled down as:

$$I_{vsc,d}^{ref} = I_{vsc,d}^{des} \frac{I_{vsc,dq}^{\max}}{I_{vsc,dq}^{des}} \tag{11}$$

$$I_{vsc,q}^{ref} = I_{vsc,q}^{des} \frac{I_{vsc,dq}^{\max}}{I_{vsc,dq}^{des}} \tag{12}$$

Another type of current limiter technique gives priority to $I_{vsc,d}^{des}$ over $I_{vsc,q}^{des}$, which translates into a priority for the control of active power [18]. This technique avoids an overcurrent scenario by constraining the converter current according to the manner in which the overcurrent occurs. In case of a violation of $I_{vsc,d}^{des}$ through the *d*-axis component, i.e., $\left| I_{vsc,d}^{des} \right| > I_{vsc,d}^{\max}$, where $I_{vsc,d}^{\max}$ is set to a given percent value of $I_{vsc,dq}^{\max}$, e.g., 95%, the value of $I_{vsc,d}^{ref}$ is given by $I_{vsc,d}^{ref} = I_{vsc,d}^{\max} sign\left(I_{vsc,d}^{des}\right) = 0.95 I_{vsc,dq}^{\max} sign\left(I_{vsc,d}^{des}\right)$; otherwise, $I_{vsc,d}^{ref} = I_{vsc,d}^{des}$. Once the value of $I_{vsc,d}^{ref}$ has been computed, the maximum absolute value of $I_{vsc,q}^{\max}$

is obtained by $I_{vsc,q}^{\max}=\sqrt{\left(I_{vsc,dq}^{\max}\right)^2-\left(I_{vsc,d}^{ref}\right)^2}$. Based on this limit, if $\left|I_{vsc,q}^{des}\right|>I_{vsc,q}^{\max}$, then $I_{vsc,q}^{ref}=I_{vsc,q}^{\max}sign\left(I_{vsc,q}^{des}\right)$; otherwise, $I_{vsc,q}^{ref}=I_{vsc,q}^{des}$. The geometric representation of this technique is shown in Fig. 3(b).

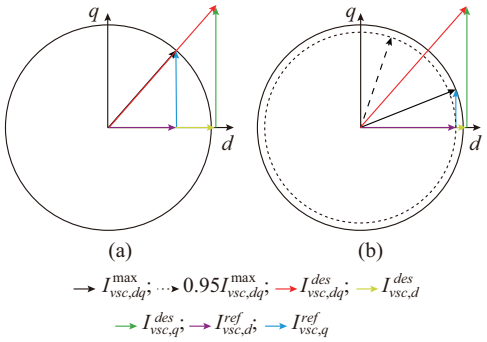

Fig. 3. Current limiter techniques. (a) Vector limiter. (b) Active power priority.

2) Power-based Converter Operational Limits

Once the values of $I_{vsc,d}^{ref}$ and $I_{vsc,q}^{ref}$ have been obtained, it is possible to specify the converter operational limits in terms of active and reactive power instead of currents. In this case, the allowable range of values for $P_{viac'}$ is defined as $-1.5V_{vi,d}\left|I_{vsc,d}^{ref}\right|\le P_{viac'}\le 1.5V_{vi,d}\left|I_{vsc,d}^{ref}\right|$. When the reactor resistance is neglected, it results in $P_{acvi}=-P_{viac'}$, which means that $-1.5V_{vi,d}\left|I_{vsc,d}^{ref}\right|\le P_{acvi}\le 1.5V_{vi,d}\left|I_{vsc,d}^{ref}\right|$, i. e., $P_{acvi}^{\max}=1.5V_{vi,d}\left|I_{vsc,d}^{ref}\right|$. Based on the aforementioned, the reactive power limits of converter are computed by:

$$Q_{vsc}^{\max}=Q_{acvi}^{\max}=\sqrt{\left(V_{ac}I_{vsc}^{\max}\right)^2-\left(P_{acvi}^{\max}\right)^2} \tag{13}$$

$$Q_{vsc}^{\min}=Q_{acvi}^{\min}=-\sqrt{\left(V_{ac}I_{vsc}^{\max}\right)^2-\left(P_{acvi}^{\max}\right)^2} \tag{14}$$

Finally, the converter losses are computed as $P_{loss}=P_{dcac}-P_{acvi}$ such that the limits of the active power entering the DC node are given by:

$$P_{dcac}^{\max}=P_{loss}+P_{acvi}^{\max} \tag{15}$$

$$P_{dcac}^{\min}=P_{loss}+P_{acvi}^{\min} \tag{16}$$

III. Complementarity Constraints

The double-sided inequality constraints representing the VSC operational limits are included in the proposed formulation of the power flow problem by using complementarity constraints and the FBMF. To achieve this goal, inequality constraints are transformed into equality constraints as follows. First, the double-sided inequality constraints are expressed mathematically by two complementarity constraints, each of which is then transformed into a nonlinear equality constraint using the FBMF. Then, the two equality constraints are directly included in the power flow problem.

The complementarity constraint $0\le a\perp b\ge 0$ states that the product of the two variables a and b must be 0 (i.e., $ab=0$) while satisfying the conditions $a\ge 0$ and $b\ge 0$. This condition can be expressed as an equality constraint by using the FBMF [21] such that:

$$0\le a\perp b\ge 0\Leftrightarrow\varphi(a,b)=\sqrt{a^2+b^2}-(a+b)=0 \tag{17}$$

The manner in which $\varphi(a,b)$ is formulated depends on the physical limits that it represents.

A VSC can adjust one of its state variables x_{adj} within limits $x_{adj}^{\min}\le x_{adj}\le x_{adj}^{\max}$ to maintain the value of another variable fixed at a given set point $y_{cont}=y_{cont}^{sp}$. However, when x_{adj} reaches one of its limits, x_{adj} is fixed at the violated limit, and the controlled variable y_{cont} is no longer regulated, and therefore $y_{cont}\ne y_{cont}^{sp}$. This behavior can be captured by the set of complementarity constraints of (18) under the assumption that when $x_{adj}=x_{adj}^{\max}$ ($x_{adj}=x_{adj}^{\min}$), $y_{cont}<y_{cont}^{sp}$ ($y_{cont}>y_{cont}^{sp}$).

$$\begin{cases}0\le\left(x_{adj}-x_{adj}^{\min}\right)\perp\left(y_{cont}-y_{cont}^{sp}\right)\ge 0\\ 0\le\left(x_{adj}^{\max}-x_{adj}\right)\perp\left(y_{cont}^{sp}-y_{cont}\right)\ge 0\end{cases} \tag{18}$$

However, (18) does not entirely satisfy the complementarity constraint conditions when the violation of one limit occurs. This is due to the set of equations associated with a double-sided inequality constraint with only one controlled variable, where only one of the equations in (18) satisfies those conditions. This drawback is overcome by defining two independent complementarity auxiliary variables: $x_{cont-}^{cc}=y_{cont}-y_{cont}^{sp}$ and $x_{cont+}^{cc}=y_{cont}^{sp}-y_{cont}$. Thus, (18) can be expressed as (19), which can then be transformed into a set of two equality constraints (20) by using the FBMF.

$$\begin{cases}0\le\left(x_{adj}-x_{adj}^{\min}\right)\perp x_{cont-}^{cc}\ge 0\\ 0\le\left(x_{adj}^{\max}-x_{adj}\right)\perp x_{cont+}^{cc}\ge 0\end{cases} \tag{19}$$

$$\begin{cases}\sqrt{\left(x_{adj}-x_{adj}^{\min}\right)^2+\left(x_{cont-}^{cc}\right)^2}-\left(x_{adj}-x_{adj}^{\min}\right)-\left(x_{cont-}^{cc}\right)=0\\ \sqrt{\left(x_{adj}^{\max}-x_{adj}\right)^2+\left(x_{cont+}^{cc}\right)^2}-\left(x_{adj}^{\max}-x_{adj}\right)-\left(x_{cont+}^{cc}\right)=0\end{cases} \tag{20}$$

The pair of equality constraints in (20) representing the double-sided inequality constraint $x_{adj}^{\min}\le x_{adj}\le x_{adj}^{\max}$ is directly incorporated into the set of power flow mismatch equations. The resultant set of nonlinear equations is entirely determined by adding x_{cont-}^{cc} and x_{cont+}^{cc} to the set of state variables to be solved in the power flow problem. In this case, x_{cont-}^{cc} and x_{cont+}^{cc} are initialized at 0 such that the complementarity constraint conditions are satisfied when x_{adj} is within limits.

Finally, a value bigger than 0 of one of these auxiliary variables indicates the extent to which the controlled variable y_{cont} deviates from its target value. This also indicates that the adjusted variable x_{adj} has been set at the corresponding limit. Since only one limit can be violated, one of the following two conditions are satisfied. If $x_{cont-}^{cc}>0$, then $x_{adj}=x_{adj}^{\min}$, $x_{cont+}^{cc}=0$, and $x_{adj}<x_{adj}^{\max}$; if $x_{cont+}^{cc}>0$, then $x_{adj}=x_{adj}^{\max}$, $x_{cont-}^{cc}=0$, and $x_{adj}>x_{adj}^{\min}$. Note that in both cases, the complementary constraint conditions are satisfied.

A. Complementarity-based VSC Limits

In this proposal, the operating state of each VSC is constrained to $m_a^{\min}\le m_a\le m_a^{\max}$ and $Q_{vsc}^{\min}\le Q_{vsc}\le Q_{vsc}^{\max}$. On the other hand, all VSCs using the phase angle for controlling the active power $P_{dcac}^{sp}(\boldsymbol{x})$, excluding those working in the V_{dc}^{sp} or

AC_{slack} control mode, are also constrained to satisfy $V_{dc}^{\min} \le V_{dc} \le V_{dc}^{\max}$ and $P_{dcac}^{\min} \le P_{dcac}(\boldsymbol{x}) \le P_{dcac}^{\max}$.

Based on the information mentioned above, the set of equality constraints representing the double-sided inequality constraints associated with m_a, Q_{vsc}, and V_{dc} in $\boldsymbol{x}$, and $P_{dcac}(\boldsymbol{x})$ are given by (21)-(24), respectively.

$$\begin{cases} \sqrt{\left(m_a - m_a^{\min}\right)^2 + \left(x_{m_a-}^{cc}\right)^2} - \left(m_a - m_a^{\min}\right) - x_{m_a-}^{cc} = 0 \\ \sqrt{\left(m_a^{\max} - m_a\right)^2 + \left(x_{m_a+}^{cc}\right)^2} - \left(m_a^{\max} - m_a\right) - x_{m_a+}^{cc} = 0 \end{cases} \tag{21}$$

$$\begin{cases} \sqrt{\left(Q_{vsc} - Q_{vsc}^{\min}\right)^2 + \left(x_{Q_{vsc}-}^{cc}\right)^2} - \left(Q_{vsc} - Q_{vsc}^{\min}\right) - x_{Q_{vsc}-}^{cc} = 0 \\ \sqrt{\left(Q_{vsc}^{\max} - Q_{vsc}\right)^2 + \left(x_{Q_{vsc}+}^{cc}\right)^2} - \left(Q_{vsc}^{\max} - Q_{vsc}\right) - x_{Q_{vsc}+}^{cc} = 0 \end{cases} \tag{22}$$

$$\begin{cases} \sqrt{\left(V_{dc} - V_{dc}^{\min}\right)^2 + \left(x_{V_{dc}-}^{cc}\right)^2} - \left(V_{dc} - V_{dc}^{\min}\right) - x_{V_{dc}-}^{cc} = 0 \\ \sqrt{\left(V_{dc}^{\max} - V_{dc}\right)^2 + \left(x_{V_{dc}+}^{cc}\right)^2} - \left(V_{dc}^{\max} - V_{dc}\right) - x_{V_{dc}+}^{cc} = 0 \end{cases} \tag{23}$$

$$\begin{cases} \sqrt{\left(P_{dcac}(\boldsymbol{x}) - P_{dcac}^{\min}\right)^2 + \left(x_{P_{dcac}-}^{cc}\right)^2} - \left(P_{dcac}(\boldsymbol{x}) - P_{dcac}^{\min}\right) - x_{P_{dcac}-}^{cc} = 0 \\ \sqrt{\left(P_{dcac}^{\max} - P_{dcac}(\boldsymbol{x})\right)^2 + \left(x_{P_{dcac}+}^{cc}\right)^2} - \left(P_{dcac}^{\max} - P_{dcac}(\boldsymbol{x})\right) - x_{P_{dcac}+}^{cc} = 0 \end{cases} \tag{24}$$

B. Complementarity-based Generator Limits

A generator connected to the i^{th} node can adjust its reactive power within limits $Q_{Gen,i}^{\min} \le Q_i^{Gen}(\boldsymbol{x}) \le Q_{Gen,i}^{\max}$ to maintain its nodal voltage magnitude fixed at a given setpoint $V_i = V_i^{sp}$. To handle these limits, $Q_i^{Gen}(\boldsymbol{x})$ is explicitly expressed as the difference between the demanded and calculated injections of reactive power at the generator node. Thus, the pair of equality constraints in (25) can be readily incorporated into the set of power flow mismatch equations:

$$\begin{cases} \sqrt{\left(Q_i^{Gen}(\boldsymbol{x}) - Q_{Gen,i}^{\min}\right)^2 + \left(x_{Gen,i-}^{cc}\right)^2} - \left(Q_i^{Gen}(\boldsymbol{x}) - Q_{Gen,i}^{\min}\right) - x_{Gen,i-}^{cc} = 0 \\ \sqrt{\left(Q_{Gen,i}^{\max} - Q_i^{Gen}(\boldsymbol{x})\right)^2 + \left(x_{Gen,i+}^{cc}\right)^2} - \left(Q_{Gen,i}^{\max} - Q_i^{Gen}(\boldsymbol{x})\right) - x_{Gen,i+}^{cc} = 0 \end{cases} \tag{25}$$

C. Complementarity-based Control Constraints

The control of a state variable x_i or a function of state variables $g_i(\boldsymbol{x})$ is mathematically represented by complementarity-based control constraints, which must consider the existing relationship between the outer controls and inner current control in the case of VSCs. This means that the constraints must consider the proper limits of the state variables that are adjusted for achieving the specified control target together with the limits associated with the VSC operational condition.

1) Modulation Index Based Control Constraints

When the VSC modulation index is used to achieve the V_{vi}^{sp} control mode, the voltage magnitude to be controlled is solved as a state variable in the power flow formulation, i.e., $V_{vi} \subset \boldsymbol{x}$, subjected to the following complementarity-based control constraint:

$$V_{vi} = V_{vi}^{sp} + x_{m_a-}^{cc} - x_{m_a+}^{cc} + x_{Q_{vsc}-}^{cc} - x_{Q_{vsc}+}^{cc} \tag{26}$$

In this case, if m_a has a value above its maximum limit at a given iteration of the solution process, its value steers towards $m_a^{\max}$ during the remaining iterations required to solve the power flow problem. Thus, at the power flow solution, the final values of the variables composing (26) are $V_{vi} < V_{vi}^{sp}$, $m_a = m_a^{\max}$, $x_{m_a+}^{cc} > 0$, and $x_{m_a-}^{cc} = x_{Q_{vsc}-}^{cc} = x_{Q_{vsc}+}^{cc} = 0$.

A similar reasoning applies when $m_a < m_a^{\min}$ during the solution of the power flow problem. In this solution, $V_{vi} > V_{vi}^{sp}$.

Since the tuning of m_a modifies the amount of reactive power produced by the VSC to achieve the V_{vi}^{sp} control mode, this reactive power could violate one of its bounds because of an overcurrent condition. In this case, the target control is not achieved even though $m_a^{\min} < m_a < m_a^{\max}$. This operating condition is mathematically represented by including the auxiliary variables $x_{Q_{vsc}-}^{cc}$ and $x_{Q_{vsc}+}^{cc}$ associated with the VSC reactive power limits in (26). Thus, if $Q_{vsc} = Q_{vsc}^{\max}$ ($Q_{vsc} = Q_{vsc}^{\min}$), the corresponding auxiliary variable has a value of $x_{Q_{vsc}+}^{cc} > 0$ ($x_{Q_{vsc}-}^{cc} > 0$), which results in a voltage magnitude of $V_{vi} < V_{vi}^{sp}$ ($V_{vi} > V_{vi}^{sp}$).

The aforementioned operating rationale is also applied when m_a is tuned to control $Q_{viac}(\boldsymbol{x})$ at a specified value Q_{viac}^{sp}, resulting in the following control constraint:

$$-Q_{viac}(\boldsymbol{x}) = -Q_{viac}^{sp} + x_{m_a-}^{cc} - x_{m_a+}^{cc} + x_{Q_{vsc}-}^{cc} - x_{Q_{vsc}+}^{cc} \tag{27}$$

2) VSC Phase Angle Based Control Constraints

The P_{dcac}^{sp} control mode performed by modulating the VSC phase angle is represented by:

$$P_{dcac}(\boldsymbol{x}) = P_{dcac}^{sp}(\boldsymbol{x}) + x_{V_{dc}+}^{cc} - x_{V_{dc}-}^{cc} + x_{P_{dcac}-}^{cc} - x_{P_{dcac}+}^{cc} \tag{28}$$

The amount of active power $P_{dcac}(\boldsymbol{x})$ injected from the DC grid into the DC side of VSC is composed of two terms that directly depend on the value of the converter DC voltage V_{dc}. The first term causes $P_{dcac}(\boldsymbol{x})$ to increase linearly with V_{dc}, whereas the second term causes $P_{dcac}(\boldsymbol{x})$ to decrease quadratically with V_{dc}. Thus, an increment (decrement) in the value of V_{dc} will reduce (increase) the amount of active power $P_{dcac}(\boldsymbol{x})$ exchanged between the DC grid and VSC. Within the context of this control mode, this implies that if V_{dc} violates one of its limits because of the network operating conditions, the active power $P_{dcac}(\boldsymbol{x})$ will have a lower or higher value with respect to the target control. Thus, if $V_{dc} = V_{dc}^{\max}$ ($V_{dc} = V_{dc}^{\min}$), the value of $P_{dcac}(\boldsymbol{x})$ will satisfy $P_{dcac}(\boldsymbol{x}) > P_{dcac}^{sp}(\boldsymbol{x})$ ($P_{dcac}(\boldsymbol{x}) < P_{dcac}^{sp}(\boldsymbol{x})$). This is why the auxiliary variables $x_{V_{dc}-}^{cc}$ and $x_{V_{dc}+}^{cc}$ are included in (28). However, the inner current control can limit the amount of active power flowing through the converter to avoid an overcurrent condition such that the auxiliary variables $x_{P_{dcac}-}^{cc}$ and $x_{P_{dcac}+}^{cc}$ must also be included in (28).

Finally, when the converter phase angle is used to perform the V_{dc}^{sp} or AC_{slack} control mode, (28) is replaced by (29) or (30), respectively.

$$V_{dc} = V_{dc}^{sp} \tag{29}$$

$$\phi = 0 \tag{30}$$

3) Reactive Power Based Control Constraint of Generator

Regarding the control of voltage magnitudes by synchronous generators, the control constraint at the i^{th} node, referred to as the *PV* node, is given by:

$$V_i = V_i^{sp} + x_{Gen,i-}^{cc} - x_{Gen,i+}^{cc} \tag{31}$$

When the generator reaches its limit $Q_{Gen,i}^{\max}$ ($Q_{Gen,i}^{\min}$), $x_{Gen,i+}^{cc} > 0$, $x_{Gen,i-}^{cc} = 0$ ($x_{Gen,i-}^{cc} > 0, x_{Gen,i+}^{cc} = 0$) and $V_i < V_i^{sp}$ ($V_i > V_i^{sp}$).

IV. Multi-terminal AC-DC Power Flow Problem

The generalized power flow model for a multi-terminal AC-DC system can be categorized into AC grids and DC grids.

A. AC grids

In the proposed formulation, the magnitudes and phase angles of voltages associated with the set of all AC nodes $\mathcal{N}_{AC}$ are considered with unknown state variables to be solved, that is, V_i and θ_i in $\boldsymbol{x}$, $\forall i \in \mathcal{N}_{AC}$.

However, the pair of nodal equality constraints used in the power flow formulation depends on the manner in which each node is defined. In this context, the conventional active and reactive power mismatch equations (32) and (33) are used for the set of all nonregulated nodes $\mathcal{N}_{AC}^{PQ} \subseteq \mathcal{N}_{AC}$, referred to as *PQ* nodes, excluding the AC nodes of converters.

$$\Delta P_i = P_i^{Gen} - P_i^{Load} - V_i \sum_{j \in \mathcal{N}_{AC}} V_j \left(G_{ij} \cos\left(\theta_i - \theta_j\right) + B_{ij} \sin\left(\theta_i - \theta_j\right) \right) = 0 \quad \forall i \in \mathcal{N}_{AC}^{PQ} \tag{32}$$

$$\Delta Q_i = Q_i^{Gen} - Q_i^{Load} - V_i \sum_{j \in \mathcal{N}_{AC}} V_j \left(G_{ij} \sin\left(\theta_i - \theta_j\right) - B_{ij} \cos\left(\theta_i - \theta_j\right) \right) = 0 \quad \forall i \in \mathcal{N}_{AC}^{PQ} \tag{33}$$

The active power mismatch equation (32) is the only one considered for the set $\mathcal{N}_{AC}^{PV} \subseteq \mathcal{N}_{AC}$ composed of all *PV* nodes except the slack node:

$$\Delta P_i = 0 \quad \forall i \in \mathcal{N}_{AC}^{PV} \tag{34}$$

On the other hand, the reactive power mismatch equation (33) is replaced by the voltage magnitude control constraint (31). Note that for this type of node, the reactive power mismatch equation (33) is implicitly satisfied through (25).

The pair of constraints associated with the set of slack nodes $\left(\mathcal{N}_{AC}^{S} \subseteq \mathcal{N}_{AC}\right)$ is given by:

$$\theta_i = \theta_i^{ref} \quad \forall i \in \mathcal{N}_{AC}^{S} \tag{35}$$

$$V_i = V_i^{sp} \quad \forall i \in \mathcal{N}_{AC}^{S} \tag{36}$$

The power mismatch constraints for the set of AC nodes of converters $\left(\mathcal{N}_{AC}^{ac} \subseteq \mathcal{N}_{AC}\right)$ are given by:

$$\Delta P_{vsc} = P_{acdc,i}(\boldsymbol{x}) + P_{acvi,i}(\boldsymbol{x}) = 0 \quad \forall i \in \mathcal{N}_{AC}^{ac} \tag{37}$$

$$\Delta Q_{vsc} = Q_{vsc,i} - Q_{acvi,i}(\boldsymbol{x}) = 0 \quad \forall i \in \mathcal{N}_{AC}^{ac} \tag{38}$$

where $P_{acdc,i}(\boldsymbol{x})$, $P_{acvi,i}(\boldsymbol{x})$, and $Q_{acvi,i}(\boldsymbol{x})$ are given by (3), (7), and (8), respectively. In addition, $Q_{vsc,i}$ in $\boldsymbol{x}$ is a state variable for the i^{th} converter.

Finally, the constraint that ensures the null exchange of reactive power between the DC and AC networks is given by:

$$\phi = \theta_{ac} \tag{39}$$

B. DC Grids

Assuming that the network is composed of a set of nodes $\mathcal{N}_{DC}$. All nodal voltage magnitudes are state variables to be solved in the power flow problem: U_i in $\boldsymbol{x}$, $\forall i \in \mathcal{N}_{DC}^{P}$, $\mathcal{N}_{DC}^{P} \subseteq \mathcal{N}_{DC}$; $V_{dc,i}$ in $\boldsymbol{x}$, $\forall i \in \mathcal{N}_{DC}^{dc}, \mathcal{N}_{DC}^{dc} \subseteq \mathcal{N}_{DC}$. Depending on the type of node, one single nodal constraint is defined as follows.

The active power mismatch constraint that must be satisfied is given by:

$$\Delta P_{i,DC}^{dc} = P_{dc,i}^{Load} + V_{dc,i} \left(\sum_{j \in \mathcal{N}_{DC}^{P}} U_j G_{ij} + \sum_{j \in \mathcal{N}_{DC}^{dc}} V_{dc,j} G_{ij} \right) + P_{dcac}(\boldsymbol{x}) = 0 \quad \forall i \in \mathcal{N}_{DC}^{dc} \tag{40}$$

where $P_{dcac,i}(\boldsymbol{x})$ is computed from (1) for the i^{th} converter.

For the remaining nodes composing the set $\mathcal{N}_{DC}^{P}$, the active power mismatch equations are given by:

$$\Delta P_i^{DC} = -P_i^{Gen} + P_i^{Load} + U_i \left(\sum_{j \in \mathcal{N}_{DC}^{P}} U_j G_{ij} + \sum_{j \in \mathcal{N}_{DC}^{dc}} V_{dc,j} G_{ij} \right) = 0 \quad \forall i \in \mathcal{N}_{DC}^{P} \tag{41}$$

Finally, the duty cycle D in $\boldsymbol{x}$ of the DC-DC converters is associated with the converter capacity for controlling the active power injected into one of its terminals [20]. Thus, the following constraint equation must be included in the power flow formulation if a converter connecting nodes k and m performs this type of control:

$$P_{mk} = U_m^2 (2/R) - U_m U_k (2D/R) = -P_m^{sp} \tag{42}$$

C. Unified Power Flow Solution

Table I summarizes the set of nonlinear nodal mismatch equations $\boldsymbol{f}(\boldsymbol{x}) = \boldsymbol{0}$, given by (21)-(42), and the vector of state variables $\boldsymbol{x} = \left[\boldsymbol{\theta}_{AC}, \boldsymbol{V}_{AC}, \boldsymbol{V}_{DC}, \boldsymbol{\phi}, \boldsymbol{m}_a, \boldsymbol{Q}_{vsc}, \boldsymbol{D}, \boldsymbol{x}^{cc} \right]^{\mathrm{T}}$ used in the formulation of the multi-terminal AC-DC power flow problem.

TABLE I
State Variables and Mismatch Equations for Proposed AC-DC Power Flow Approach

State variable	Mismatch equation	State variable	Mismatch equation
$\boldsymbol{x}_{ma}^{cc}$	(21)	$\boldsymbol{\theta}_{AC}^{PQ}$	(32)
$\boldsymbol{x}_{Q_{VSC}}^{cc}$	(22)	$\boldsymbol{V}_{AC}^{PQ}$	(33)
$\boldsymbol{x}_{V_{dc}}^{cc}$	(23)	$\boldsymbol{\theta}_{AC}^{PV}$	(34)
$\boldsymbol{x}_{P_{dcac}}^{cc}$	(24)	$\boldsymbol{\theta}_{AC}^{Slack}$	(35)
$\boldsymbol{x}_{Gen}^{cc}$	(25)	$\boldsymbol{V}_{AC}^{Slack}$	(36)
$\boldsymbol{m}_a^{V}$	(26)	$\boldsymbol{V}_{AC}^{ac}$	(37)
$\boldsymbol{m}_a^{Q}$	(27)	$\boldsymbol{Q}_{VSC}$	(38)
$\boldsymbol{\phi}^{P}$	(28)	$\boldsymbol{\theta}_{AC}^{ac}$	(39)
$\boldsymbol{\phi}^{V}$	(29)	$\boldsymbol{V}_{DC}$	(40)
$\boldsymbol{\phi}^{Slack}$	(30)	$\boldsymbol{U}$	(41)
$\boldsymbol{V}_{AC}^{PV}$	(31)	D	(42)

Note that some vectors of $\boldsymbol{x}$ can be expressed as: $\boldsymbol{x}^{cc} = \left[\boldsymbol{x}_{Gen}^{cc}, \boldsymbol{x}_{m_a}^{cc}, \boldsymbol{x}_{Q_{vsc}}^{cc}, \boldsymbol{x}_{V_{dc}}^{cc}, \boldsymbol{x}_{P_{dcac}}^{cc} \right]$; $\boldsymbol{\theta}_{AC} = \left[\boldsymbol{\theta}_{AC}^{Slack}, \boldsymbol{\theta}_{AC}^{PV}, \boldsymbol{\theta}_{AC}^{PQ}, \boldsymbol{\theta}_{AC}^{ac} \right]$; $\boldsymbol{V}_{AC} = \left[\boldsymbol{V}_{AC}^{Slack}, \boldsymbol{V}_{AC}^{PV}, \boldsymbol{V}_{AC}^{PQ}, \boldsymbol{V}_{AC}^{ac} \right]$; $\boldsymbol{V}_{DC} = \left[\boldsymbol{V}_{dc}, \boldsymbol{U} \right]$; $\boldsymbol{m}_a = \left[\boldsymbol{m}_a^{V}, \boldsymbol{m}_a^{Q} \right]$; and $\boldsymbol{\phi} =$

$[\boldsymbol{\phi}^P, \boldsymbol{\phi}^V, \boldsymbol{\phi}^{Slack}]$. The solution of the power flow problem is obtained by iteratively solving $\boldsymbol{f}(\boldsymbol{x})=\boldsymbol{0}$ for $\Delta\boldsymbol{x}^k$ in the linearized problem $\boldsymbol{J}^k\Delta\boldsymbol{x}^k=-\boldsymbol{f}(\boldsymbol{x}^k)$, where $\boldsymbol{J}$ is the Jacobian matrix. From a given set of initial conditions $\boldsymbol{x}^0$, all state variables are updated at each iteration k, i.e., $\boldsymbol{x}^{k+1}=\boldsymbol{x}^k+\Delta\boldsymbol{x}^k$, until the maximum absolute value of $\boldsymbol{f}(\boldsymbol{x}^{k+1})$ is less than a specified tolerance *tol* or until the maximum number of iterations $R^{\max}$ has been achieved. Finally, the unified power flow solution mentioned above is schematically summarized in Fig. 4.

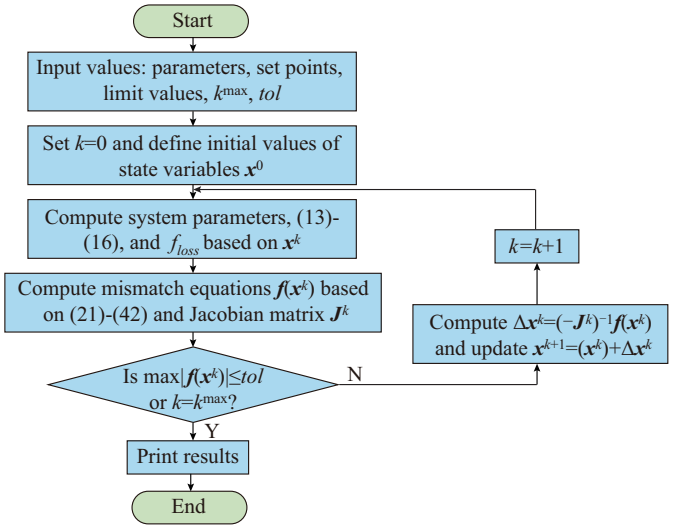

Fig. 4. Unified power flow solution.

V. Case Studies

The effectiveness of the proposed approach is numerically demonstrated by using the CIGRE test system [20] as shown in Fig. 5, the IEEE RTS-96 system with the inclusion of two MTDC systems as shown in Fig. 6, and a modified 7791-bus large-scale system. The proposed approach is implemented in the MATLAB® platform using a Lenovo P71 with an Intel® Xeon® CPU E3-1505Mv6@3 GHz.

A. CIGRE Test System

In the proposed approach, the power flow study of the CIGRE test system is performed by considering the same current capacity reported in [20] for all converter stations. The parameters corresponding to the transformers, filters, and reactors of the VSC-based AC-DC station model detailed in Section II are $\bar{Y}_T=100-\mathrm{j}10000$, $\bar{Y}_{sf}=\mathrm{j}0.05$, and $\bar{Y}_{pr}=-\mathrm{j}1000$. The remaining system parameters are the ones given in [20]. The total numbers of nodes for the AC and DC systems are 33 and 15, respectively. The 11 VSC-based converter stations linking the AC and DC networks are operating in the control modes given in Fig. 5, while the two DC-DC converter stations are operating in the active power control mode. The converters connected to *dc* nodes 34 and 36 operate under the *V-P* droop control with reference voltages at 1 p.u. and 0.99 p.u., respectively. The active power is controlled by these converters at 350 MW and −120 MW, respectively. In Fig. 5, the blue voltage magnitude results are from the base case and the green ones from the limited case.

The converters connected to *dc* nodes 37 and 46 operate under the *V-P* droop control with a dead band from 0.98 p.u. to 1 p.u., reference voltages of 0.99 p.u., and set points of active power control of 800 MW and 1500 MW, respectively. In addition, the converter connected to *dc* node 42 uses a *V-I* droop with a reference voltage of 1.01 p.u. and a reference current of −5.9406 p.u.. For all droop controls, the slope is $1/(10P_{nom})$. In addition, the power losses of six VSCs are given by $f_{loss}=a+bI_{vsc}+cI_{vsc}^2$, where a is 1% of the converter nominal power P_{nom}, b is 0.3% of the converter nominal voltage V_{nom}, and $c=0.01V_{nom}^2/P_{nom}$ [8], [19]. These VSCs are identified in Fig. 5 with the symbol f_{loss}. Finally, the modulation index and DC voltage in all VSCs are limited to $0.77\le m_a\le 0.86$ and $0.95\ \text{p.u.}\le V_{dc}\le 1.05\ \text{p.u.}$, respectively.

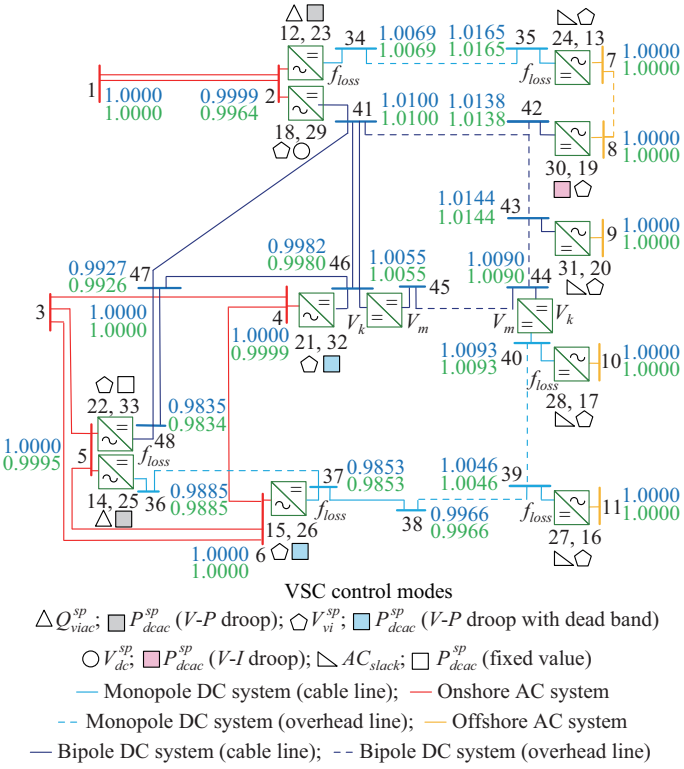

Fig. 5. CIGRE test system.

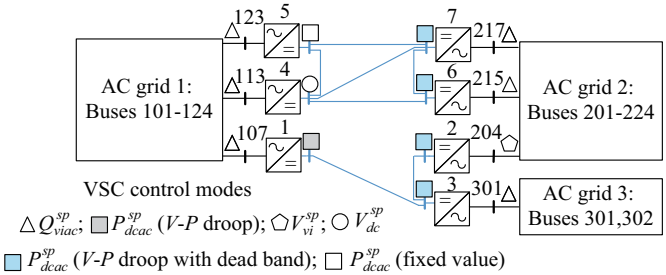

Fig. 6. Modified RTS-96 system.

The power flow solution converges in four iterations and 0.06 s to a tolerance of 1×10^{-6}, with all converters operating within the specified limits listed in Table II. The nodal voltage magnitudes obtained with the proposed approach are shown in Fig. 5. Finally, the active and reactive power exchanged between the DC and AC systems are reported in columns 5 and 6 of Table II, respectively.

TABLE II
OPERATING CONDITIONS OF CIGRE TEST SYSTEM

Nodes			Base case (without limits enforced)				Limited case			
dc	*ac*	*vi*	m_a	P_{dcac} (MW)	Q_{viac} (Mvar)	P_{loss} (MW)	m_a	P_{dcac} (MW)	Q_{viac} (Mvar)	P_{loss} (MW)
34	23	12	0.8147	405.46	0	11.13	0.8119	405.46	0	11.15
35	24	13	0.7988	–410.34	31.56	11.50	0.7988	–410.34	23.61	11.50
36	25	14	0.8245	–132.37	0	8.67	0.8200	–132.37	450.05	12.29
37	26	15	0.8342	800.00	–18.25	19.42	0.8342	800.00	–19.80	19.42
39	27	16	0.8076	–487.37	–0.25	12.63	0.8076	–487.37	–0.25	12.63
40	28	17	0.8130	102.80	–0.01	2.80	0.8130	102.80	–0.01	2.80
41	29	18	0.8029	–2019.70	–141.18	19.72	0.8000	–2049.30	–156.90	20.36
42	30	19	0.7998	–571.80	-39.63	4.98	0.7998	–571.80	–28.08	4.98
43	31	20	0.7999	–992.09	-1.00	7.90	0.7999	–992.09	–1.00	7.90
46	32	21	0.8233	1500.00	–22.25	11.62	0.8236	1528.86	–26.56	11.97
48	33	22	0.8362	1700.00	–19.31	14.16	0.8400	1700.00	–466.02	14.05

B. Handling of Limits

In this case study of the CIGRE test system, the operating conditions of three converter stations are modified with respect to the base case used to demonstrate numerically the manner in which limit violations are correctly detected and enforced using complementarity constraints. The limits of these converters are changed as shown in Table III.

TABLE III
NEW CONVERTER LIMITS FOR CIGRE TEST SYSTEM

Nodes			Parameter	Converter limits	
dc	*ac*	*vi*		Original limit	New limit
36	25	14	$m_a^{\max}$	0.86	0.820
41	29	18	$m_a^{\max}$	0.86	0.800
46	32	21	$V_{dc}^{\max}$	1.05	0.998

The power flow solution is obtained in seven iterations to a tolerance of 1×10^{-6}, where the results for the AC-DC converter stations are reported in columns 8-11 of Table II. These clearly show that two converters operate at their corresponding maximum modulation index values. In this case, the modulation indices of converters at *vi* nodes 14 and 18 operate at their limits of 0.82 and 0.80, respectively, and yield uncontrolled voltage magnitudes of $V_{14}=0.9941$ p.u. and $V_{18}=0.9897$ p.u., respectively, instead of a target value of 1 p.u. for both voltages. Finally, the converter connected at dc node 46 is forced to operate at its upper value of DC voltage such that the operating control mode $P_{dcac}^{sp}(\boldsymbol{x})$ is no longer achieved. In this case, the active power exchanged between the DC and AC grids is $P_{dcac}^{46\text{-}32}=1528.86$ MW instead of the target value of $P_{dcac}^{46\text{-}32,sp}(\boldsymbol{x})=1500$ MW. As expected, the active power exchanges between the DC and AC systems change with respect to the base case, as could be deduced by comparing the results shown in Table II.

Finally, this case study has been newly solved by the proposed approach but by using an alternative iterative solution method based on a robust projected Levenberg-Marquardt (PLM) algorithm [22]. The power flow solution is obtained in 10 iterations by considering a damping factor of $\nu=1\times10^{-8}$ and a tolerance to the convergence of 1×10^{-6}. An analysis of this solution clearly shows that the same results reported in columns 8-11 of Table II are obtained.

C. Comparison with Other Unified Models

This section presents numerical comparisons of the results obtained by the proposed approach and a similar unified model proposed in [13]. Because of droop control strategies, the handling of limits and the relationships between outer and inner controls are not considered in [13]. Thus, the control specifications for the base case of CIGRE test system are defined to yield a fair comparison. The converters connected at *dc* nodes 34, 36, and 41 operate under the DC slack control strategy with set points of 1 p.u., 0.99 p.u., and 1.01 p.u., respectively. In addition, the converters connected at *dc* nodes 37, 42, 46, and 48 have a specified active power control of 800, –600, 1500, and 1700 MW, respectively, whereas the converters at *dc* nodes 35, 39, 40, and 43 operate as AC slack nodes. Finally, converters at *vi* nodes 12 and 14 have a specified voltage control at 1 p.u..

The results obtained with the proposed model and [13] are reported in columns 3-5 and 6-8 of Table IV, respectively.

TABLE IV
COMPARISON BETWEEN UNIFIED MODEL APPROACHES

Nodes		Proposed model			Model in [13]		
dc	*vi*	m_a	P_{dcac} (MW)	Q_{kvi} (Mvar)	m_a	P_{dcac} (MW)	Q_{kvi} (Mvar)
34	12	0.8203	384.8	3.90	0.8205	385.7	1.3
35	13	0.8027	–389.3	31.80	0.8028	–390.2	31.7
36	14	0.8232	–121.9	–1.22	0.8225	–121.3	7.4
37	15	0.8363	800.0	–17.70	0.8363	800.0	–17.8
39	16	0.8066	–496.1	0	0.8066	–493.6	0
40	17	0.8110	100.7	0	0.8110	100.6	0
41	18	0.8292	–1991.7	–140.60	0.8288	–1990.7	–137.2
42	19	0.8035	–600.0	–39.40	0.8035	–600.0	–39.2
43	20	0.8035	–992.2	0	0.8035	–993.1	0
46	21	0.8335	1500.0	–20.10	0.8335	1500.0	–20.3
48	22	0.8488	1700.0	–15.30	0.8495	1700.0	–24.3

By comparing both solutions, it clearly shows that the results are very similar in the modulation indices and active power flows but with differences in the amount of reactive power Q_{kvi}, which are caused by the manner in which each model represents the reactive power generation of converter. Note that Q_{kvi} corresponds to the reactive power that flows through the transformer in converter station, as shown in Fig. 1. Finally, the other comparisons between the VSC model and power flow formulation proposed in our approach and [13] are explicitly reported in Section I.

D. Modified IEEE RTS-96 System

The performance of the proposed approach is assessed by analyzing the IEEE RTS-96 system with the inclusion of two MTDC systems [23]. In this case, the AC system is divided into three independent AC grids by removing the transmission lines interconnecting nodes 107-203, 113-215, and 123-217. These nodes are then used to interconnect the AC grids through two MTDC systems, which results in the AC-MTDC system shown in Fig. 6. The system parameters as well as the coefficients associated with the power loss function of each converter are the same as those reported in [23]. The VSCs 5 and 7 have a maximum current rating $I_{vsc}^{\max}$ of 0.5 and 0.7 p.u., respectively. This current $I_{vsc}^{\max}$ has a value of 1.1 p.u. for VSCs 1 and 2, whereas $I_{vsc}^{\max}$ equals 2.2 p.u. for the remaining converters. In addition, the voltage magnitude at the AC side of converters is limited to 1.2 p.u.. For the sake of clarity, the control modes of converters and their corresponding set points are reported in columns 2 and 3 of Table V. The set of VSCs 1, 2, and 7 operates under the *V-P* droop control mode with a slope of 1/11, whereas VSCs 3 and 6 operate under this same control mode but with a slope of 1/22. In addition, the dead band associated with the *V-P* droop control of VSCs 2, 3, 6, and 7 is ±0.01 p.u. with respect to the reference voltage V_{dc}^{ref}.

TABLE V
VSC CONTROL MODES AND COMPARISON BETWEEN METHODS

VSC	Control by ϕ	Control by m_a	Results obtained by proposed approach and [23]
1	VP^D, $V_1^{ref}=1$, $P_{1\text{-}107}^{sp}(V_1^{ref})=58$	$Q_{107}^{sp}=50$	$P_{1\text{-}107}=59.33$, $P_{loss}=1.58$, $V_1=1.001$, $V_{ac}=1.152$, $Q_{107\text{-}ac}=50$, $V_{107}=1.032$
2	VP_{db}^D, $V_2^{ref}=1$, $P_{2\text{-}204}^{sp}(V_2^{ref})=77$	$V_{204}^{sp}=1$	$P_{2\text{-}204}=77$, P_{loss}=1.73, $V_2=0.998$, $V_{ac}=0.953$, $Q_{204\text{-}ac}=-20.82$, $V_{204}=1$
3	VP_{db}^D, $V_3^{ref}=1.01$, $P_{3\text{-}301}^{sp}(V_3^{ref})=-138$	$Q_{301}^{sp}=130$	$P_{3\text{-}301}=-138$, P_{loss}=3.94, $V_3=1.012$, $V_{ac}=1.2$, $Q_{301\text{-}ac}=114.02$, $V_{301}=1.051$
4	DC Slack, $V_4^{sp}=1$	$Q_{113}^{sp}=75$	$P_{4\text{-}113}=113.59$, $P_{loss}=2.89$, $V_4=1$, $V_{ac}=1.125$, $Q_{113\text{-}ac}=75$, $V_{113}=1.02$
5	$P_{5\text{-}123}^{sp}=-50$	$Q_{123}^{sp}=20$	$P_{5\text{-}123}=-47.91$, $P_{loss}=1.38$, $V_5=1.014$, $V_{ac}=1.101$, $Q_{123\text{-}ac}=18.01$, $V_{123}=1.05$
6	VP_{db}^D, $V_6^{ref}=1.02$, $P_{6\text{-}215}^{sp}(V_6^{ref})=-120$	$Q_{215}^{sp}=0$	$P_{6\text{-}215}=-120$, $P_{loss}=2.94$, $V_6=1.018$, $V_{ac}=1.026$, $Q_{215\text{-}ac}=0$, $V_{215}=1.014$
7	VP_{db}^D, $V_7^{ref}=1.01$, $P_{7\text{-}217}^{sp}(V_7^{ref})=52$	$Q_{217}^{sp}=20$	$P_{7\text{-}127}=52$, $P_{loss}=1.35$, $V_7=1.01$, $V_{ac}=1.098$, $Q_{217\text{-}ac}=20$, $V_{217}=1.04$

The power flow solution is obtained by the proposed approach in 10 iterations and 0.2 s to a convergence tolerance of 10^{-6}. The results associated with the control modes and power losses of VSCs are reported in column 4 of Table V. To validate the use of complementarity constraints for handling both the operational limits and control modes of converters, the power flow simulation is repeated but by using MatACDC software [23] based on the sequential AC-DC approach reported in [5]. In this case, the solution requires six sequential AC-DC iterations, which takes 0.43 s to converge to a tolerance of 10^{-6}, with a total number of 19, 10, and 6 iterations for the AC grids 1, 2, and 3, respectively. In this sequential process, the same results are obtained but with the handling of VSC limits performed by using if-based conditional tests. The results reported in Table V clearly show that VSC 5 hits its current limit at 0.5 p.u. such that the power control targets are not achieved. Furthermore, VSC 3 hits its upper AC voltage limit of 1.2 p.u., which corresponds to a modulation index limit of 0.9646 in the proposed approach, such that the reactive power control is not achieved. These results confirm the suitability of the proposed approach for automatically handling operational limits in the power flow problem. Finally, a comparison of the nodal voltage profile obtained by the proposed approach and that obtained from [5] indicates that the maximum absolute differences in the voltage magnitudes and phase angles are 7.801×10^{-8} p.u. and $(2.325\times10^{-5})°$, respectively.

E. Large-scale System Case

The proposed approach has been applied to a 7791-bus model of a large-scale interconnected power system consisting of seven regional transmission control areas. This system is composed of 7747 AC buses, 44 DC buses, 482 generator buses, 3493 load buses, 4182 transmission lines, and 4524 transformers. In this case, the 21 tie-lines interconnecting the seven regional control areas plus the 22 most important transmission lines of the system, are replaced by 11 point-to-point HVDC links and six DC multi-terminal networks. The solution for this system converges in seven iterations and 55 s to meet a tolerance of 1×10^{-4}. In this case, four converters violate one of their operational limits according to the specified control modes, with one converter set at its lower DC voltage limit and one fixed at its maximum modulation index, while the iterative solution process enforces the current limits for the other two converters.

VI. CONCLUSION

A comprehensive and flexible model of a VSC converter suitable for VSC-MTDC power flow studies is introduced in this paper. The model incorporates the outer and inner current control loops of the VSC for correct representation of its steady-state operating point. Several operational control modes are defined using the outer control schemes, which supply the current references to the inner current control

loop. The inner current control loop is used to prevent over-current operating conditions. This is accomplished by constraining the current of AC converter using a vector-form control or by giving priority to the control of active power.

The concept of complementarity constraints and the FBMF are combined to represent directly the operating and physical limits of synchronous generators and VSCs in the power flow formulation. The formulation enables the automatic enforcement of violated limits during the iterative process of the power flow solution. In addition, complementarity-based control constraints are introduced to represent the specified VSC control modes of operation as well as the interactions between the various controls and their limits. The functionality of the VSC model and complementary constraints is demonstrated by numerical examples.

REFERENCEES

[1] B. Mitra, B. Chowdhury, and M. Manjrekar, "HVDC transmission for access to off-shore renewable energy: a review of technology and fault detection techniques," *IET Renewable Power Generation*, vol. 12, no.13, pp. 1563-1571, Sept. 2018.

[2] C. Angeles-Camacho, O. L. Tortelli, E. Acha *et al*., "Inclusion of a high voltage DC-voltage source converter model in a Newton-Raphson power flow algorithm," *IEE Proceedings – Generation, Transmission and Distribution*, vol. 150, no. 6, pp. 691-696, Nov. 2003.

[3] X. -P. Zhang, "Multiterminal voltage-sourced converter-based HVDC models for power flow analysis," *IEEE Transactions on Power Systems*, vol. 19, no. 4, pp. 1877-1884, Nov. 2004.

[4] A. Pizano-Martinez, C. R. Fuerte-Esquivel, H. Ambriz-Perez *et al*., "Modeling of VSC-based HVDC systems for a Newton-Raphson OPF algorithm," *IEEE Transactions on Power Systems*, vol. 22, no. 4, pp. 1794-1803, Nov. 2007.

[5] J. Beerten, S. Cole, and R. Belmans, "Generalized steady-state VSC MTDC model for sequential AC/DC power flow algorithms," *IEEE Transactions on Power Systems*, vol. 27, no. 2, pp. 821-829, May 2012.

[6] M. Z. Kamh and R. Iravani, "Steady-state model and power-flow analysis of single-phase electronically coupled distributed energy resources," *IEEE Transactions on Power Delivery*, vol. 27, no. 1, pp. 131-139, Jan. 2012.

[7] Q. H. Nguyen, G. Todeschini, and S. Santoso, "Power flow in a multi-frequency HVac and HVdc system: formulation, solution, and validation," *IEEE Transactions on Power Systems*, vol. 34, no. 4, pp. 2487-2497, Jul. 2019.

[8] S. Khan and S. Bhowmick, "A generalized power-flow model of VSC-based hybrid AC-DC systems integrated with offshore wind farms," *IEEE Transactions on Sustainable Energy*, vol. 10, no. 4, pp. 1775-1783, Oct. 2019.

[9] Y. Ye, Y. Qiao, L. Xie *et al*., "A comprehensive power flow approach for multi-terminal VSC-HVDC system considering cross-regional primary frequency responses," *Journal of Modern Power Systems and Clean Energy*, vol. 8, no. 2, pp. 238-248, Mar. 2020.

[10] E. Karami, G. B. Gharehpetian, H. Mohammadpour *et al*., "Generalised representation of multi-terminal VSC-HVDC systems for AC-DC power flow studies," *IET Energy Systems Integration*, vol. 2, no. 1, pp. 50-58, Mar. 2020.

[11] E. Acha and B. Kazemtabrizi, "A new STATCOM model for power flows using the Newton-Raphson method," *IEEE Transactions on Power Systems*, vol. 28, no. 3, pp. 2455-2465, Aug. 2013.

[12] E. Acha, B. Kazemtabrizi, and L. M. Castro, "A new VSC-HVDC model for power flows using the Newton-Raphson method," *IEEE Transactions on Power Systems*, vol. 28, no. 3, pp. 2602-2612, Aug. 2013.

[13] E. Acha and L. M. Castro, "A generalized frame of reference for the incorporation of, multi-terminal VSC-HVDC systems in power flow solutions," *Electric Power Systems Research*, vol. 136, pp. 415-424, Jul. 2016.

[14] G. Díaz and C. González-Morán, "Fischer-Burmeister-based method for calculating equilibrium points of droop-regulated microgrids," *IEEE Transactions on Power Systems*, vol. 27, no. 2, pp. 959-967, May 2012.

[15] L. Sundaresh and P. N. Rao, "A modified Newton-Raphson load flow scheme for directly including generator reactive power limits using complementarity framework," *Electric Power Systems Research*, vol. 109, pp. 45-53, Apr. 2014.

[16] Y. Ju, J. Wang, Z. Zhang *et al*., "A calculation method for three-phase power flow in micro-grid based on smooth function," *IEEE Transactions on Power Systems*, vol. 35, no. 6, pp. 4896-4903, Nov. 2020.

[17] R. Tapia-Juárez, C. R. Fuerte-Esquivel, E. Espinosa-Juárez *et al*., "Steady-state model of grid-connected photovoltaic generation for power flow analysis," *IEEE Transactions on Power Systems*, vol. 33, no. 5, pp. 5727-5737, Sept. 2018.

[18] T. M. Haileselassie, "Control, dynamics and operation of multi-terminal VSC-HVDC transmission systems," Ph.D. dissertation, Department of Electric Power Engineering, Norwegian University of Science and Technology, Trondheim, Norway, 2012.

[19] A. Yazdani and R. Iravani, *Voltage-sourced Converters in Power Systems: Modeling, Control, and Applications*. New Jersey: Wiley, 2010.

[20] T. K. Vrana, Y. Yang, D. Jovcic *et al*., "The CIGRE B4 DC grid test system," *Electra*, vol. 270, no. 1, pp. 10-19, Jan. 2013.

[21] A. Fischer, "A special newton-type optimization method," *Optimization*, vol. 24, no. 3-4, pp. 269-284, Mar. 1992.

[22] Y. Ju, J. Wang, and Z. Zhang, "An improved power flow method to cope with non-smooth constraints of integrated energy systems," *CSEE Journal of Power and Energy Systems*, Early Access, pp. 1-10, Aug. 2020.

[23] J. Beerten, MatACDC. (2021, Feb.). [Online]. Available: http://www.esat.kuleuven.be/electa/teaching/matacdc/

Ricardo Martínez-Parrales received his B. Eng. and M. Sc. (Summa Cum Laude) degrees in electronic engineering from the Instituto Tecnológico de Morelia, Morelia, México, in 2005 and 2014, respectively, and his Ph.D. degree from the Universidad Michoacana de San Nicolás de Hidalgo, Morelia, México, in 2019. He is currently an Assistant Professor with the Universidad Michoacana de San Nicolás de Hidalgo and with the Instituto Tecnológico de Morelia. His research interests include the steady-state and dynamic analysis of power systems.

Claudio R. Fuerte-Esquivel received the Ph.D. degree from the University of Glasgow, Glasgow, U.K., in 1997. He is currently a Full-time Professor with the Universidad Michoacana de San Nicolás de Hidalgo, Morelia, México. He is a Member of the Mexican Academy of Science. His current research interests include the flexible AC transmission systems and critical infrastructures.

Boris A. Alcaide-Moreno received the M.Sc. degree from the Instituto Tecnológico de Morelia, Morelia, México, in 2004, and the Ph.D. degree from the Universidad Michoacana de San Nicolás de Hidalgo, Morelia, México, in 2016. He is currently the Head of the Department of Real-time Operational Security and Market Applications, National Energy Control Center, International Organization for Standardization (ISO), Mexico City, México. His current research interests include power system state estimation, security, and monitoring.

Enrique Acha received the B. Eng. degree from Universidad Michoacana, Morelia, México, in 1979, and the Ph.D. degree from the University of Canterbury, Christchurch, New Zealand, in 1988. He was a Professor of Electrical Power Systems, University of Glasgow, Glasgow, U.K., from 2001 to 2011. He is currently an Emeritus Professor of Electrical Power Systems, Tampere University, Tampere, Finland. His research interests include power electronics modeling and applications in electrical power system.